

Microscopic mechanisms of glasslike lattice thermal conductivity in tetragonal α -CsCu₅Se₃Qing-Yu Xie,^{1,2} Peng-Fei Liu,^{1,3} Jiang-Jiang Ma,^{1,3} Li-Ming Wu,^{4,5} Kai-Wang Zhang,^{2,*} and Bao-Tian Wang^{1,3,6,†}¹*Institute of High Energy Physics, Chinese Academy of Science, Beijing 100049, China*²*School of Physics and Optoelectronics, Xiangtan University, Xiangtan 411105, China*³*Spallation Neutron Source Science Center, Dongguan 523803, China*⁴*Center for Advanced Materials Research, Beijing Normal University, Zhuhai, Zhuhai 519087, China*⁵*College of Chemistry, Beijing Normal University, Beijing 100875, China*⁶*Collaborative Innovation Center of Extreme Optics, Shanxi University, Taiyuan 030006, China*

(Received 15 February 2023; revised 2 May 2023; accepted 21 June 2023; published 10 July 2023)

Understanding and predicting the anharmonic lattice dynamics of complex strongly anharmonic crystals has long been a significant challenge in condensed matter physics and materials physics. Here, we study the underlying physical principles of the ultralow glasslike κ_L in tetragonal α -CsCu₅Se₃ by combining self-consistent phonon theory and the unified thermal transport theory of crystal and glass in the framework of the Peierls-Boltzmann transport equation and first-principles anharmonic lattice dynamics. We consider the impacts of both phonon broadening by three-phonon (3ph) interaction and phonon frequency anharmonic renormalization by quartic anharmonicity on the contributions from the particlelike phonon wave packet and wavelike phonon channel transport. The strong anharmonic renormalization leads to continuous temperature-induced hardening of the acoustic modes and low-lying optical modes, which is mainly associated with the tetrahedrally coordinated rattlinglike vibrations of the Cu3 atoms. This hardening effect reduces the phonon linewidths in the low-energy area via decreasing the available 3ph scattering phase space, thus partially counteracting the decreased impact on κ_L by increasing the phonon population and yielding a weak temperature-dependent κ_L . Furthermore, the strong phonon broadening results in the coherent thermal transport channel that stems from the coherent coupling between different vibration eigenstates. Upon heating, the off-diagonal terms in the heat-flux operator become quite significant and dominate the phonon thermal transport process, suggesting the qualitative breakdown of the traditional phonon gas model in complex disordered crystals. In this paper, we provide the physical microscopic mechanisms of the glasslike κ_L in complex host-guest systems and highlight the influence of the lattice anharmonicity on thermal conductivity.

DOI: [10.1103/PhysRevB.108.014302](https://doi.org/10.1103/PhysRevB.108.014302)**I. INTRODUCTION**

Materials exhibiting ultralow lattice thermal conductivity (κ_L) have been widely applied in diverse fields, such as thermal barrier coatings in aerospace engines and high-performance thermoelectric devices [1,2]. The paradigm of phonon glass and electron crystal (PGEC), wherein thermal conductivity behaves as amorphous solids or glasses yet preserves good electrical transport properties, has supplied explicit instruction to improve the thermal-to-electric energy conversion in the thermoelectric field [3,4]. The investigation of the microscopic mechanism of glasslike thermal conductivity in ordered compounds not only can unravel complex anharmonic lattice dynamics but also can provide criteria to design a generation of high-performance thermoelectric materials [5–13].

However, a fundamental understanding of the underlying physical microscopic mechanisms of the ultralow glasslike κ_L in complex severely anharmonic materials is a great challenge

in condensed matter and material physics [14]. Generally, the host-guest structure, the guest atoms (rattlers) loosely bound inside oversized hosts [15–17], should exhibit the typical character of PGEC. Historically, the ultralow κ_L in such a host-guest structure has been ascribed to the resonant scatterings between the localized rattling and acoustic modes, which reduces the phonon lifetimes in the low frequencies near the avoided-crossing points [15]. However, a theoretical study in skutterudites showed that the reduction of κ_L originates from the increased three-phonon (3ph) scattering rate due to filler-induced modification of the phonon dispersion [18]. On the other hand, an inelastic neutron scattering study in clathrate Ba₈Ga₃Ge₃₀ showed that the impact of rattlers on κ_L mainly decreases the acoustic phonon group velocity at the avoided-crossing points, not reducing the phonon lifetime [19]. Finally, this conflict has been resolved by theoretical calculations in filled and empty clathrates. Tadano *et al.* [8] and Tadano and Tsuneyuki [9] explained that the rattlers lead to a tenfold reduction in phonon lifetimes, whereas the impact on group velocity is less significant. The reduction of phonon lifetimes is over a wide frequency range, indicating the failure of phonon-resonant scattering. The anomalous temperature-dependent thermal conductivity in host-guest systems has

*kwzhang@xtu.edu.cn

†wangbt@ihp.ac.cn

been attributed to the coupling strength between rattlers and cages [20,21] and the magnitude of static or dynamic disorders [20,22].

Theoretically, harmonic approximation fails to describe the anharmonic lattice dynamics in severely anharmonic systems. The phonon modes where mean free paths (MFPs) approach the Ioffe-Regel limit [23] (i.e., the smallest atomic distance) could not be considered normal phonons, leading to a breakdown of the conventional phonon gas model [24]. Some theoretical models have attempted to explain the weak temperature dependence of κ_L , such as the two-channel phonon transport mode. In this model, the phonon modes with MFPs shorter than the Ioffe-Regel limit should be regarded as hopping modes that obey Einstein or Cahill-Watson-Pohl models of thermal conductivity [5,13,24,25]. To some extent, the two-channel model compensates for the lack of theory on experimental data and caters to a weak temperature dependence [24]. However, some open questions remain. What is the interaction between the normal phonons and the hopping modes, and what role does this interaction play in thermal transport? Fortunately, recent theoretical and computational developments enable anharmonic phonon frequency renormalization arising from the high-order phonon-phonon interactions [11,26–30] as well as the contributions originating from the coherent coupling between different vibration eigenstates [12,31,32].

Tetragonal α -CsCu₅Se₃ is a good case study for this more general framework due to the challenges arising from (i) the presence of a large unit cell, (ii) the rattling effect in the host-guest system, (iii) massive phonon imaginary modes, and (iv) strong high-order anharmonicity [33]. These features may lead to the invalidation of the Peierls-Boltzmann transport equation (PBTE). The results of such investigations can deepen the understanding of lattice dynamics and thermal transport properties. In this paper, we investigate the origin of the glasslike ultralow κ_L in tetragonal α -CsCu₅Se₃ using first-principles-based self-consistent phonon calculations and the advanced unified thermal transport model. Results show that (i) quartic anharmonicity induces the continuing phonon frequency hardening with temperature increasing, decreasing the 3ph scattering rate via reducing the 3ph scattering weighted phase space in the low-energy area, and (ii) strong phonon broadening leads to the breakdown of the phonon quasiparticle physical picture, manifesting in glasslike κ_L dominated by coherent thermal conductivity.

II. COMPUTATIONAL METHODS

A. Density functional theory calculations

All our density functional theory (DFT) [34] calculations are performed using the projector augmented-wave [35] potentials as implemented in VASP [36]. The PBEsol form of the general gradient approximation is utilized to deal with the exchange-correlation energy functional [37]. PBEsol stands for PBE functional revised for solids, and it is a better choice for calculating structural properties closer to the experimental values. We treat the Cs ($5s^25p^66s^1$), Cu ($3d^{10}s^1$), and Se ($4s^24p^4$) shells as valence states. A kinetic energy cutoff of 500 eV and a $4 \times 4 \times 12$ Monkhorst-Pack k -point mesh are

adopted to sample the Brillouin zone for structural optimization. A tight convergence criterion of 10^{-5} eV/Å is set for the Hellman-Feynman forces acting on each atom, and the convergence criterion of the total energy is set as 10^{-8} eV. Our optimized structural parameters in the tetragonal $P4_2/mmm$ (No. 136) symmetry ($a = b = 13.04$ Å, $c = 3.97$ Å) are in good agreement (absolute error $< 2\%$) with the experimentally reported values ($a = b = 13.26$ Å, $c = 4.07$ Å) [33].

B. Estimation of force constants

The harmonic interaction force constants (IFCs) are obtained through the finite-displacement approach [38] as implemented in the PHONOPY package [39], using a $1 \times 1 \times 3$ supercell containing 108 atoms with a $4 \times 4 \times 4$ k mesh. For the anharmonic IFC calculations, since the conventional finite-displacement method tends to consume costly computation, we employ the compressive sensing lattice dynamics (CSLD) method [26–28] to obtain them. In CSLD, the compressive sensing technique [40] is utilized to select the physically important terms to obtain the cubic and quartic IFCs. To obtain the physically relevant atomic displacement, we perform *ab initio* molecular dynamics (AIMD) simulations for a $1 \times 1 \times 3$ supercell with a $1 \times 1 \times 1$ k -point grid at 300 K. The loose convergence criterion for electronic self-consistent field cycles of 10^{-4} eV is chosen since we are interested in training structures, not accurately obtaining the energy and force or verifying thermodynamic stability [26]. The AIMD simulations are conducted 3500 times in the canonical ensemble (NVT) using a Nosé-Hoover thermostat and a 1 fs time step. Then we sample 70 structures that are equally spaced in time by skipping the first 700 steps from the trajectories. We have demonstrated that 70 different configurations are enough for the anharmonic force constant calculations in the Supplemental Material (SM) [41]. To decrease cross-correlations between the sampled configurations, we use the quasirandom displacement method to displace all the atoms for all the samples with 0.1 Å [26]. Subsequently, we perform high-precision single-point energy calculations on these samples by using a $4 \times 4 \times 4$ k -mesh grid and a tight energy convergence threshold of 10^{-8} eV. Finally, we obtain the anharmonic IFCs by the least absolute shrinkage and selection operator technique [42] with a relative error of 1.74% (see Fig. S1(a) in the SM [41]). The cutoff radii of 5.29 and 4.23 Å are chosen to obtain the cubic and quartic IFCs, respectively. They are confined to the three- and four-body terms, respectively, and include interatomic interactions up to the 11th and 8th nearest neighbors, respectively.

C. Self-consistent phonon calculation

To obtain the temperature-dependent phonon dispersion curves, we solve the self-consistent phonon theory (SCPH) equations using the extracted 0 K harmonic and anharmonic IFCs. The resultant SCPH equation in the diagonal form, which considers the first-order perturbation of the phonon self-energy from the quartic anharmonicity, can be expressed as [9,29]

$$\Omega_{\mathbf{q}}^2 = \omega_{\mathbf{q}}^2 + 2\Omega_{\mathbf{q}}I_{\mathbf{q}}, \quad (1)$$

where $\omega_{\mathbf{q}}$ is the harmonic phonon frequency, and $\Omega_{\mathbf{q}}$ is the anharmonically renormalized phonon frequency at finite temperature (T). The quantity $I_{\mathbf{q}}$ is defined as

$$I_{\mathbf{q}} = \frac{1}{2} \sum_{\mathbf{q}'} \frac{\hbar \Phi(\mathbf{q} : -\mathbf{q} : \mathbf{q}' : -\mathbf{q}')}{4\Omega_{\mathbf{q}}\Omega_{\mathbf{q}'}} [1 + 2n(\Omega_{\mathbf{q}'})], \quad (2)$$

where \hbar and Φ are the reduced Planck constant and the reciprocal representation of the quartic IFCs, respectively. Here, $n(\omega) = 1/[\exp(\hbar\omega/k_B T) - 1]$ is the phonon population that obeys the Bose-Einstein statistic. Evidently, the temperature-induced effects include the phonon population. In addition, the cubic anharmonic IFCs are not considered for the correction of the harmonic IFCs since their contributions have been found to be less significant than the phonon frequency hardening by the quartic anharmonicity in some of the low κ_L systems, such as PbTe [43], clathrates [11], and TlInTe₂ [44]. In this paper, we use the ALAMODE package to conduct the IFC and SCPH calculations [29,45].

D. Phonon transport

The lattice thermal conductivity arising from particlelike propagation of phonons is obtained by solving the PBTE within the relaxation time approximation in form [46,47]:

$$\kappa_p = \frac{1}{VN} \sum_{\mathbf{q}} C_{\mathbf{q}}(T) v_{\mathbf{q}}(T) v_{\mathbf{q}}(T) \tau_{\mathbf{q}}(T). \quad (3)$$

Here, V and N represent the volume and atomic number of the lattice, respectively, $C_{\mathbf{q}}$ is the phonon mode-specific heat, $v_{\mathbf{q}} = d\Omega_{\mathbf{q}}/d\mathbf{q}$ is the group velocity, and $\tau_{\mathbf{q}} = 1/[2\Gamma_{\mathbf{q}}(\Omega_{\mathbf{q}})]$ is the lifetime of phonon \mathbf{q} . The phonon linewidths $\Gamma_{\mathbf{q}}(\Omega_{\mathbf{q}})$, which can be obtained from the imaginary part of the phonon self-energy, result from the cubic anharmonicity and takes the form:

$$\begin{aligned} \Gamma_{\mathbf{q}}(\omega) &= \frac{\pi}{2N} \sum_{\mathbf{q}', \mathbf{q}''} \frac{\hbar |\Phi(-\mathbf{q}, \mathbf{q}', \mathbf{q}'')|^2}{8\Omega_{\mathbf{q}}\Omega_{\mathbf{q}'}\Omega_{\mathbf{q}''}} \\ &\times [(n_{\mathbf{q}'} + n_{\mathbf{q}''} + 1)\delta(\omega - \Omega_{\mathbf{q}'} - \Omega_{\mathbf{q}''}) \\ &- 2(n_{\mathbf{q}'} - n_{\mathbf{q}''})\delta(\omega - \Omega_{\mathbf{q}'} + \Omega_{\mathbf{q}''})]. \end{aligned} \quad (4)$$

The Peierls-Boltzmann transport theory, which is valid when the phonon interbranch spacings are much larger, fails to describe the phonon transport behavior of the complex system since it neglects the coherence terms, i.e., the off-diagonal terms of the heat flux operators [7,31,48,49]. The contribution to κ_L of the coherence terms becomes nonnegligible when the phonon linewidths are larger than the space of the interbranch [31]. Thus, the unified thermal transport theory of glass and crystal is employed to calculate the lattice thermal conductivity as follows:

$$\begin{aligned} \kappa_{p/c} &= \frac{\hbar^2}{k_B T^2 V N_0} \sum_{\mathbf{q}} \sum_{j, j'} \frac{\omega_{\mathbf{q}j} + \omega_{\mathbf{q}j'}}{2} v_{\mathbf{q}j} v_{\mathbf{q}j'} \\ &\otimes v_{\mathbf{q}j} v_{\mathbf{q}j'} \frac{\omega_{\mathbf{q}j} n_{\mathbf{q}j} (n_{\mathbf{q}j} + 1) + \omega_{\mathbf{q}j'} n_{\mathbf{q}j'} (n_{\mathbf{q}j'} + 1)}{4(\omega_{\mathbf{q}j} - \omega_{\mathbf{q}j'})^2 + (\Gamma_{\mathbf{q}j} + \Gamma_{\mathbf{q}j'})^2} (\Gamma_{\mathbf{q}j} + \Gamma_{\mathbf{q}j'}), \end{aligned} \quad (5)$$

$$v_{\mathbf{q}j} v_{\mathbf{q}j'} = \frac{\langle e_{\mathbf{q}j} | \frac{\partial D(\mathbf{q})}{\partial \mathbf{q}} | e_{\mathbf{q}j'} \rangle}{2\sqrt{\omega_{\mathbf{q}j} \omega_{\mathbf{q}j'}}}, \quad (6)$$

where the subscripts p and c represent propagation and coherence contributions, respectively, and $v_{\mathbf{q}ij}$ is the generalized group velocity [7]. Notably, when the second summation in Eq. (5) is performed over the diagonal terms, i.e., $j = j'$, it reduces to the PBTE equation in the conventional phonon gas model. The contribution of the off-diagonal terms to κ_L originates from the coherence coupled between different vibrational eigenstates and leads to the difference between κ_L and κ_p . In this paper, the \mathbf{q} mesh in calculations based upon PBTE as implemented in the ALAMODE package [29,45] is chosen to be $9 \times 9 \times 27$, which can achieve good convergence (see Fig. S1(b) in the SM [41]).

III. RESULTS AND DISCUSSION

A. Crystal structure and anharmonicity

The structure of tetragonal α -CsCu₅Se₃ is isostructural with the famous low thermal conductivity system of CsAg₅Te₃ ($a = b = 14.64 \text{ \AA}$, $c = 4.59 \text{ \AA}$ at room temperature) [33,50]. As shown in Fig. 1, One Cs, two Se (Se1, Se2), and three Cu (Cu1, Cu2, Cu3) inequivalent atoms are in its unit cell. The lattice constants are slightly shorter than those of CsAg₅Te₃ due to the smaller atomic radii of Cu/Se compared with Ag/Te. In tetragonal α -CsCu₅Se₃, two large open tunnels are constructed by the Cu-Se covalent networks and arranged infinitely along the c axis. These two peanut-shaped tunnels, located at the center (0.5 0.5 0.5) and at the origin (0 0 0) of the unit cell, are plugged by the large Cs atoms. The Cu-Se covalent networks comprise fourfold coordinated Cu1 and Cu3, threefold coordinated Cu2, and two inequivalent Se atoms. These kinds of networks make phonon vibrations of Cu and Se spread over almost the whole energy space from 0 to 29 meV, as indicated by the element-resolved phonon density of states (PhDOS) in Fig. 1(e). The Cu-Se bonding is relatively weak, especially for Cu3-Se bonds [33,50]. The Cs atoms are only coordinated with Se, and the Cs-Se bond length is $>3.49 \text{ \AA}$. Thus, the Cs atoms are isolated in the large tunnels, and the phonon vibrations from Cs are centralized in a narrow energy range $\sim 8 \text{ meV}$. As shown, the Cu2 atoms adopt the less common coplanar triangle coordination geometry with Cu-Se bonds of $2.39\text{--}2.54 \text{ \AA}$, while a long bond length of $\sim 2.60 \text{ \AA}$ is observed in Cu3 and Cu1 atoms. Thus, the Cu3 and Cu1 atoms are expected to be the rattling cations since they possess larger interstitial space. As indicated by our calculated harmonic phonon dispersions, the imaginary acoustic and optical modes indicate strong anharmonicity [11,29]. They are mainly associated with the rattling vibrations along the transverse direction (i.e., perpendicular to the Cu1-Se-Cs networks) of Cu3 atoms and partially by Cu1 atoms. From these structural features, the rattling modes associated with the Cu3 atoms are expected to play an essential role in its phonon transport [33,50].

B. Temperature-induced anharmonic phonon renormalization

Since strong anharmonicity can lead to phonon frequency shift and phonon states broadening [11,43], the harmonic description of phonon frequencies for the tetragonal α -CsCu₅Se₃ system becomes inappropriate. Thus, we employ

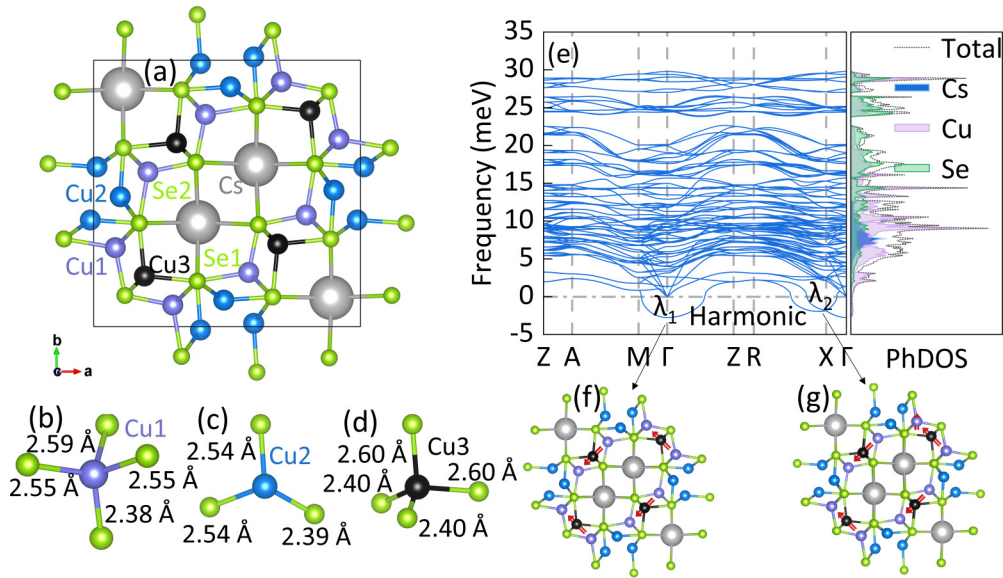


FIG. 1. Crystal structure, bonding, rattling vibrations of Cu3 atoms, and harmonic phonon dispersion curves at 0 K. (a) Top view of the crystalline structure of tetragonal α - CsCu_5Se_3 where gray, green, purple, blue, and black balls represent Cs, Se, Cu1, Cu2, and Cu3 atoms, respectively. (b)–(d) Local coordination of Cu1 (tetrahedral), Cu2 (coplanar triangle), and Cu3 (tetrahedral) atoms with bond lengths marked. (e) Harmonic phonon dispersions and corresponding element-resolved phonon density of states (PhDOS) at 0 K. (f) and (g) indicate the visualization rattling vibrations of modes associated with Cu3 atoms at Γ and X points, respectively, where the large atomic displacements are indicated by the red arrows. Here, other small atomic displacements are neglected.

the SCPH theory to treat the phonon instabilities and renormalize the phonon frequencies of tetragonal α - CsCu_5Se_3 at zero and some specific temperatures.

The anharmonically renormalized phonon dispersions of tetragonal α - CsCu_5Se_3 at different temperatures are presented in Figs. 2(a) and 2(b). When compared with the harmonic phonon dispersions, the 0 K anharmonic effects can induce the system to be dynamically stable. Increasing temperature from 0 to 300 or 700 K, the phonons in a frequency <15 meV are strongly hardened, whereas the phonons >15 meV show moderate hardening. In the phonon frequency range from 5 to 15 meV, there are many nearly dispersionless optical phonon branches that could effectively scatter the heat-carrying phonons by creating abundant scattering channels [18,51].

Generally, the acoustic phonon branches and the low-lying optical branches play a critical role in thermal transport [52–54]. Thus, we plot the dispersion curves of the two transverse acoustic modes (TA1, TA2), one longitudinal acoustic mode (LA), and two transverse optical modes (TO1, TO2) at zero temperature in Fig. 2(c). Results show that (i) there are four representative avoided-crossing points of the rattling modes between TO1 and LA and along Γ -M, Γ -Z, R-X, and Γ -X, as indicated by the black circles. Another avoided-crossing point exists between TO2 and LA and along M-A. (ii) The low-lying TO1 mode at the Γ point (Γ_{TO1}) is as low as 1.35 meV. The avoided-crossing points were believed to correlate with the phonon rattling modes and low κ_L [19,50]. The rattling vibration, which is a specific physical characteristic of PGEC [6,19], can enhance the acoustic phonon scattering and reduce κ_L , especially for host-guest systems, like clathrate $\text{Ba}_8\text{Ga}_{16}\text{Ge}_{30}$ [8,9] and cubic tetrahedrites $\text{Cu}_{12}\text{Sb}_4\text{S}_{13}$ [11]. In tetragonal α - CsCu_5Se_3 , the avoided-crossing points are

correlated with the independent rattling vibrations of the Cu3 atoms. As for the small value of Γ_{TO1} , it is smaller than or comparable with those of the famous thermoelectric materials SnSe (2.48 meV) [52], PbTe (4.10 meV) [43], MgAgSb (1.74 meV) [55], and CsAg_5Te_3 (1.86 meV) [33,50]. The low value of Γ_{TO1} generally indicates low acoustic-branch frequencies, weak chemical bonding, strong acoustic-optical coupling, strong phonon scattering, and low κ_L [56,57]. As indicated by our calculated phonon dispersions, the saturated frequencies of the acoustic branches responsible for phonon transport merely reach ~ 2.5 – 4.5 meV at 0 K and strong increase to ~ 4.5 – 7.5 meV at 700 K. Such values are comparable with those of MgAgSb (2.5–4.5 meV) [56], SnSe (1.8–6.2 meV), and PbTe (2.1–11.1 meV) [43]. The frequencies of the acoustic-optical coupling at 0 (700) K are in the range of ~ 1.3 – 4.2 (4.1–7.5) meV, which are also close to those of MgAgSb [56] and SnSe [58]. According to the anharmonicity theory, strong acoustic-optical coupling gives rise to the decay of the optical phonons into acoustic phonons, resulting in a finite lifetime for the phonons [59,60]. These features manifest strong anharmonicity in tetragonal α - CsCu_5Se_3 and are associated with the severe deviation of its κ_L from the ideal T^{-1} decay.

To further investigate the influence of the independent rattling vibrations of Cu3 atoms on phonon anharmonic renormalization, the temperature dependences of the rattling modes (TO1 and TO2) at Γ and R points, the element-resolved partial and total PhDOS at different temperatures, the temperature-dependent anisotropic mean squared displacements (MSDs) of six inequivalent atoms, and the Cu3 atom-resolved PhDOS are calculated and plotted in Fig. 2 and in Figs. S2 and S3 in the SM [41]. Results show that (i) the frequencies of TO1 and TO2 modes exhibit relatively strong anharmonic

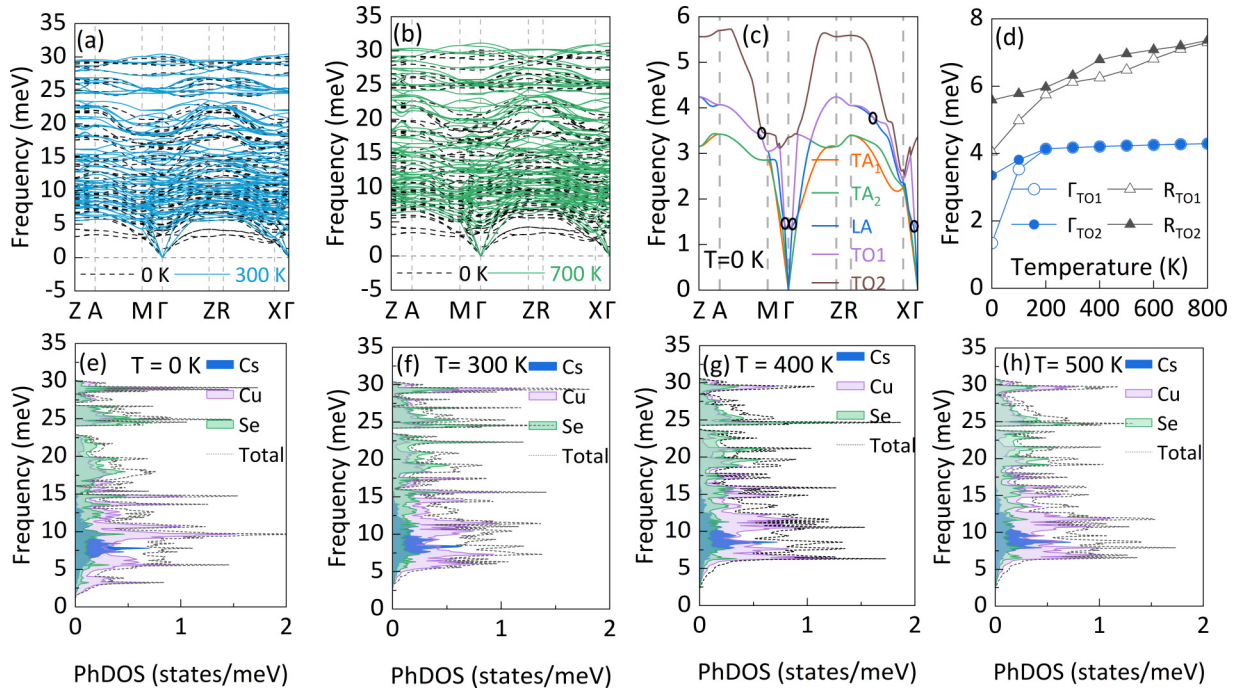


FIG. 2. Temperature-induced anharmonic phonon renormalization. (a) and (b) Anharmonically renormalized phonon dispersions of tetragonal α -CsCu₅Se₃ at 0, 300, and 700 K. (c) Acoustic (two transverse acoustic branches TA1 and TA2 and one longitudinal acoustic branch LA) and rattling optical modes (two transverse optical modes TO1 and TO2) with black circles marking the avoided crossing points along Γ -M, Γ -Z, R-X, Γ -X, and M-A. (d) Shifts of phonon frequencies for TO1 and TO2 at Γ and R points in the Brillouin zone at finite temperatures. (e)–(h) The element-resolved phonon density of states (PhDOS) at 0, 300, 400, and 500 K, respectively.

renormalization and strong temperature dependence, indicating the drastic phonon frequency hardening, especially for the TO1 mode. This kind of temperature-induced hardening of optical phonon modes has also been observed in the low- κ_L system of TlInTe₂ [44]. (ii) The phonon frequencies <7.6 meV are mainly contributed by the Cu3 atoms. This indicates that the acoustic as well as the acoustic-optical coupling phonons are mainly vibrations of the Cu3 atoms. (iii) The MSDs of the Cu3 atoms are far larger than those of other atoms, which agree well with the previous exponential study [33]. Meanwhile, the equivalent isotropic displacement parameter (U_{eq}) of different atoms varies in the order Se1 < Se2 < Cs < Cu2 < Cu1 < Cu3 both theoretically and experimentally, indicating the loose chemical bonding of Cu3-Se and the rattling characteristic [61]. The MSDs of the Cu3 atoms also show evident anisotropy: The vibration amplitudes within the ab plane are considerably larger than that along the c axis.

C. Particlelike contributions to κ_L

To reveal the phonon thermal transport mechanism in tetragonal α -CsCu₅Se₃, we start our comprehensive analysis of the calculated κ_p by solving the PBTE based on the SCPH method, which considers the phonon frequency shift and phonon broadening by anharmonic renormalization. Hereafter, we denote thermal conductivities from particlelike propagation of phonons by κ_p^\perp , κ_p^\parallel , and κ_p^{avg} , where \perp and \parallel symbols indicate components of κ_p perpendicular and parallel to the ab plane, respectively, and avg represents their average value. From Fig. 3(a), one can see that the two calculated data of κ_p^\perp and κ_p^\parallel decay with temperature as $T^{-0.17}$ and $T^{-0.11}$,

respectively, deviating from the well-known T^{-1} behavior in the conventional phonon gas model or weakly anharmonic solids [53,62]. The breakdown of the phonon gas model and the weak temperature-dependent behaviors clearly indicate strong quartic anharmonicity in tetragonal α -CsCu₅Se₃ and the necessity of anharmonic renormalization of the harmonic phonon frequencies.

To examine the phonon mode-specific contributions to κ_p , the thermal conductivity spectrum $\kappa_p(\omega)$ and its cumulative value at different temperatures are plotted in Fig. 3(b). The results illustrate that both κ_p^\perp and κ_p^\parallel are mainly contributed from the acoustic and low-lying optical modes ($\omega < 12.5$ meV). The rattling vibrations at ~ 5 meV contribute the largest peak, and the acoustic-optical coupling phonons at ~ 9 meV contribute the second largest one. The high-energy optical modes have partial contributions to κ_p^\perp but are almost neglected to κ_p^\parallel . Considering the anharmonic renormalization, the threshold that contributes most to κ_p^\parallel appears a blueshift from 12.5 (300 K) to 15 meV (400 K) but is not that evident. In the traditional phonon gas model, the phonons are regarded as particles, and it is assumed that the maximum phonon scattering rate of a phonon mode is equal to twice its frequency, as the black line shows in Fig. 3(c). Results show that the weak temperature dependence can be attributed to a balance between two effects: (i) On the one hand, the phonon population enhances with increasing temperature, resulting in larger $\Gamma_{3\text{ph}}$; (ii) however, the scattering rates $\Gamma_{3\text{ph}}$ associated with the acoustic and low-lying optical modes are strongly suppressed owing to the hardening effect by anharmonic renormalization in the frequency region <7 meV, when the temperature is increased from 300 to 500 K.

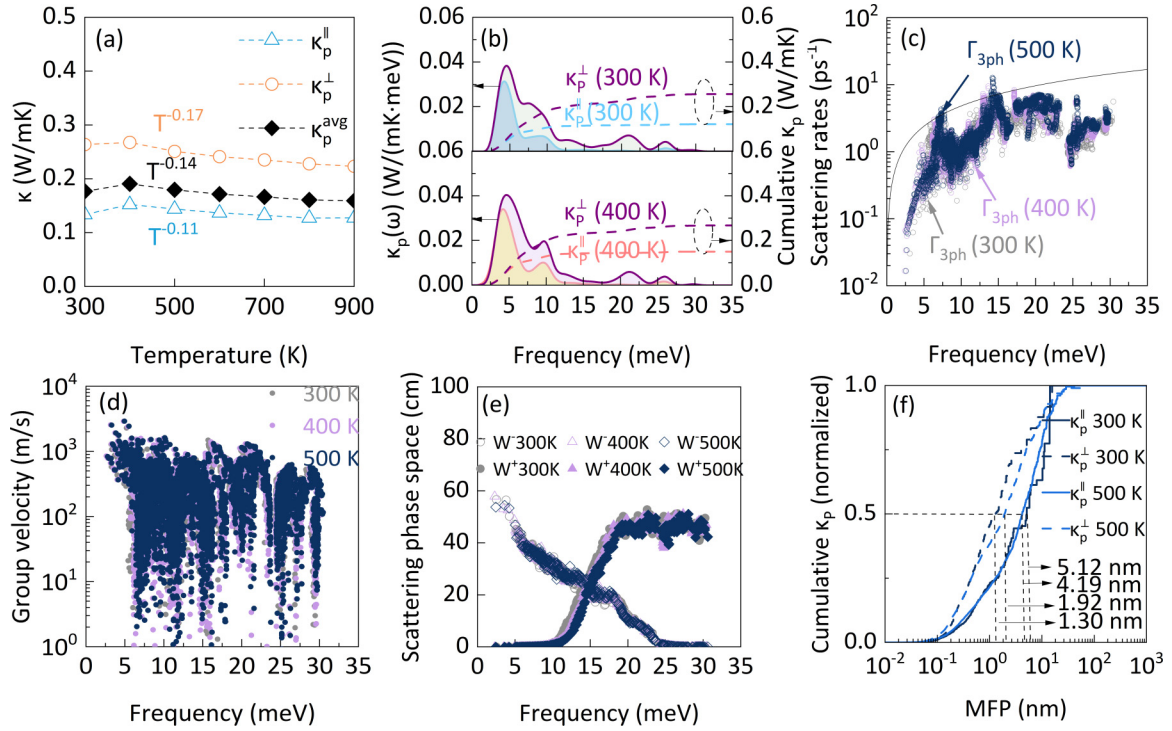


FIG. 3. Heat transport arising from particlelike propagation of phonons. (a) Particlelike contributions to the κ_L of tetragonal α -CsCu₅Se₃ based on the anharmonically renormalized [i.e., self-consistent phonon theory (SCPH)] phonon frequencies in the Peierls-Boltzmann transport equation (PBTE) work frame. κ_p^\perp and κ_p^\parallel represent the components of κ_p perpendicular and parallel to the ab plane, respectively, and κ_p^{avg} indicates their average, i.e., $\kappa_p^{\text{avg}} = (\kappa_p^\perp + 2\kappa_p^\parallel)/3$. (b) Thermal conductivity spectra $\kappa_p^\perp(\omega)$ and $\kappa_p^\parallel(\omega)$ and their cumulatives at 300 and 400 K. (c) Comparison of three-phonon (3ph) scattering rates at 300 (gray dots), 400 (purple dots), and 500 K (dark blue dots). The black line assumes that the maximum phonon scattering rate of a phonon mode equals twice its frequency [5]. (d) Comparison of phonon group velocities at 300 (gray dots), 400 (purple dots), and 500 K (dark blue dots). (e) Calculated energy- and momentum-conserving 3ph scattering phase space at finite temperatures, where the hollow and filled dots represent the combination process (W^+ : $\lambda + \lambda_1 \rightarrow \lambda_2$) and the splitting process ($\lambda \rightarrow \lambda_1 + \lambda_2$), respectively. (f) Calculated normalized cumulative κ_p as a function of mean free paths (MFPs) at $T = 300$ and 500 K.

Another key factor in determining κ_p is the phonon group velocity. As shown in Fig. 3(d), most values of the phonon group velocities are small (<1000 m/s) and can be ascribed to those dispersionless optical phonon branches. Only some values associated with the acoustic modes are up to 3000 m/s. These results are consistent with our results of the phonon spectra. Noteworthy, the phonon group velocities are weakly hardened since the effect of anharmonic renormalization on the phonon group velocities is less significant than that of the scattering rate. On the other hand, the magnitude of the scattering rates $\Gamma_{3\text{ph}}$ directly depends on the phonon scattering space and the square of the scattering matrix elements. There are two types of phonon interactions in the 3ph scattering process [51], i.e., a combination process (W^+ : $\lambda + \lambda_1 \rightarrow \lambda_2$) and a splitting process (W^- : $\lambda \rightarrow \lambda_1 + \lambda_2$), as shown in Fig. 3(e). Results show that the severe reduction of the combination process W^+ dominates over the frequency range, especially for the low-energy area, but the splitting process is inverse. The reduction of W^- is significantly stronger than that of W^+ owing to phonon frequency shift induced by anharmonic renormalization, suggesting that the impact of anharmonic renormalization on W^+ is less significant than that of W^- . Thus, we attribute the reduction in scattering rate $\Gamma_{3\text{ph}}$ to the reduced strength of the coupling between the acoustic and optical modes in the low-energy area via decreasing their

scattering phase space, in good agreement with the previous analysis of scattering rates.

To further analyze the impact of the size effect on κ_p , we plot the MFP dependence of κ_p^\perp and κ_p^\parallel at 300 and 500 K in Fig. 3(f). Results show that the short MFP phonons dominate the thermal transport in tetragonal α -CsCu₅Se₃, again suggesting the presence of strong anharmonicity. The MFPs corresponding to 50% κ_p^\perp and κ_p^\parallel are as short as 5.12 (4.19) and 1.30 (1.92) nm at 300 (500) K, respectively, indicating the weak size effect [46].

D. Wavelike contributions to κ_L

The traditional Peierls-Boltzmann theory, which is well based on the phonon quasiparticle physical picture, however, fails to explain the thermal transport property in complex multiatomic systems, strong anharmonicity systems, or the coexistence of anharmonicity and disorder (rattling effect or PGEC) because it does not account for the off-diagonal contributions of the heat-flux operator, i.e., the contribution from the heat-carrying wavelike phonons originating from the coherent coupling between different vibrational eigenstates [31,49,63]. As shown in Fig. 4, compared with κ_p , the amplitudes of κ_c are quite significant. Here, κ_c^\parallel and κ_c^\perp account for 57 and 38% contributions to that of κ_c^\parallel and κ_c^\perp at 300 K, respectively.

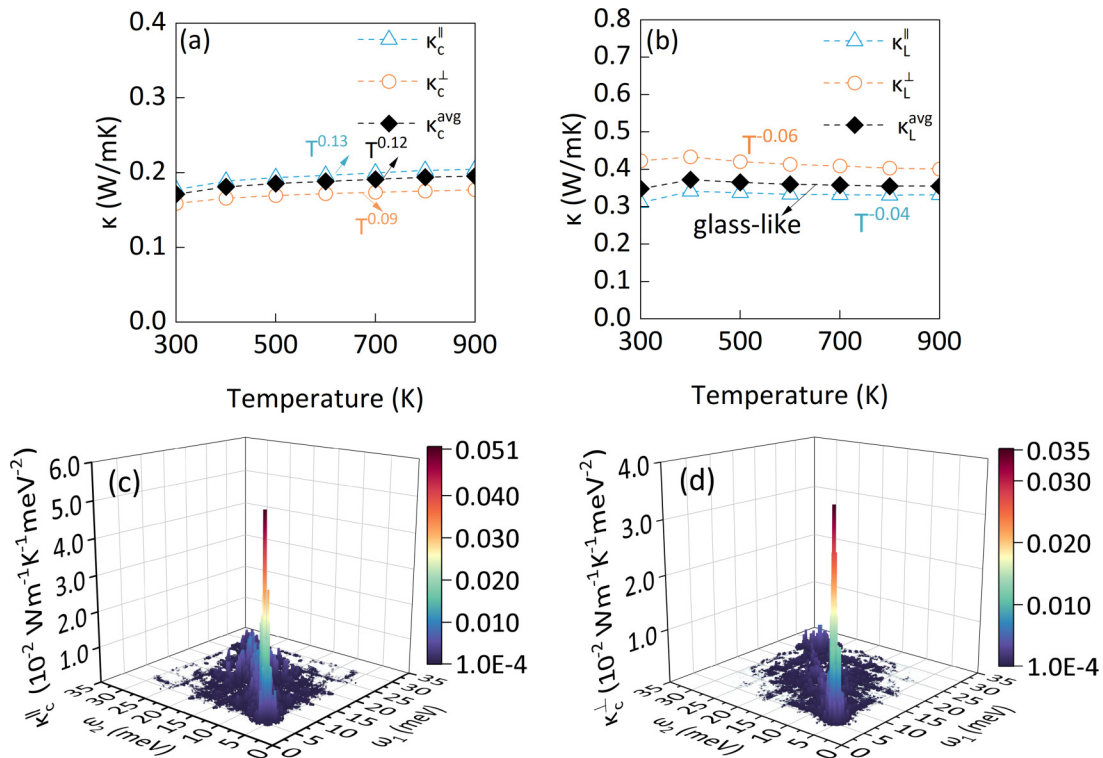


FIG. 4. Heat transport stems from wavelike tunneling of phonons. (a) Calculated coherent thermal conductivities (i.e., κ_c^{\perp} , κ_c^{\parallel} , and their average κ_c^{avg}) at different temperatures. (b) Total κ_L (i.e., $\kappa_L = \kappa_p + \kappa_c$) as a function of temperature. (c) and (d) Three-dimensional visualizations of the mode-specific contributions to the coherent thermal conductivity of κ_c^{\perp} and κ_c^{\parallel} at 300 K. A color scale corresponding to the variation of colors in (c) and (d) is shown, which has the same unit as indicated in the z axes of both figures.

Increasing temperature further enhances the proportion of κ_c in κ_L . At 1000 K, the contributions of κ_c^{\parallel} and κ_c^{\perp} are up to 62 and 45%, respectively. Importantly, both κ_c^{\perp} and κ_c^{\parallel} show positive temperature dependences upon heating and in temperature dependences that increase as $T^{0.13}$ and $T^{0.09}$, respectively. Such positive temperature-dependent behavior of κ_c has also been found in TlInTe $_2$ [44].

Interestingly, the value of κ_p^{\perp} is much larger than that of κ_p^{\parallel} , with an anisotropy ratio of 1.97 at 300 K (i.e., $\kappa_p^{\perp}/\kappa_p^{\parallel}$). However, the anisotropy of κ_c exhibits reversal with a smaller ratio of 1.11 (i.e., $\kappa_c^{\parallel}/\kappa_c^{\perp}$). The anisotropy of κ_p can be attributed to two effects: (i) open large tunnels along the z axis in tetragonal α -CsCu $_5$ Se $_3$, and (ii) the anisotropy in the phonon dispersion curves results in an anisotropy phonon group velocity. On the other hand, we note that the coherent phonon thermal transport occurs between coupled different phonon vibration eigenstates, where the generalized phonon group velocity is associated with two different frequencies (ω_1 and ω_2) [7]. Thus, the impact of the slopes of phonon branches on κ_c is less significant than that of κ_p , counteracting partial anisotropy in κ_c [44].

To further explain the opposite temperature dependences of κ_p and κ_c and how the coupled vibration eigenstates affect the wavelike phonon transport, we plot the two-dimensional density of states $\kappa_{c,\omega_1\omega_2}$ for the wavelike phonon thermal conductivities κ_c^{\parallel} and κ_c^{\perp} at 50 K (see Fig. S4 in the SM [41]) and 300 K [Figs. 4(c) and 4(d)]. The main contributions to the coherent thermal conductivity stem from phonons with very similar frequencies, i.e., quasidegenerate vibration

eigenstates. Large values of $\kappa_{c,\omega_1\omega_2}$ are mainly distributed in the diagonal area, particularly for phonons involving the Cu3 rattling vibrations in the low-energy region. Strong anharmonicity leads to an enhanced phonon broadening, and the temperature-induced hardening effect reduces the interbranch space. Thus, the off-diagonal region becomes wider at 300 K compared with the results at 50 K. The optical modes that are coupled with the acoustic modes also play a crucial role in coherent phonon thermal transport, especially for vibrations in the ab plane. As shown in Fig. 2, the optical branches < 7.5 meV are denser along Γ -X than those along Γ -Z. Therefore, the two-dimensional density of states of κ_c^{\parallel} are larger than those of κ_c^{\perp} . These results are consistent with the large Cu3 atom rattling vibrations within the ab plane.

E. Discussions

In Fig. 5, we compare our calculated κ_L with previous experimental data for tetragonal α -CsCu $_5$ Se $_3$ [33]. We also present the κ_L results of Cu $_{12}$ Sb $_5$ S $_{13}$ [11,64,65], Cu $_2$ Se [66], MgAgSb [55], and its isostructural system CsAg $_5$ Te $_3$ [50] for comparison. We note that there exists some acceptable difference in the magnitude of κ_L between our calculated (0.35–0.37 W/mK) and the experimental values (0.4–0.8 W/mK). A similar difference also appears in the complex system Cu $_{12}$ Sb $_5$ S $_{13}$ or other guest-host systems. Here, we comprehensively analyze this difference from both experimental and theoretical perspectives. From the experimental point of view, it can be ascribed to the well-known

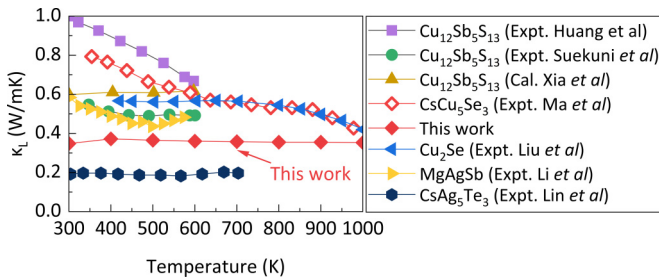


FIG. 5. Calculated κ_L of tetragonal α -CsCu₅Se₃ (red squares) in comparison with the experimental results from Ref. [33]. Experimental and theoretical results of some famous systems exhibiting glasslike κ_L , such as Cu₁₂Sb₅S₁₃ [11,64,65], MgAgSb [55], CsAg₅Te₃ [50], and Cu₂Se [66], are also presented for comparison.

experimental challenges in single crystals [19], accurate measurement of the electronic thermal conductivity [33], and extreme sensitivity of κ_L to the off-stoichiometry between various Cu atoms [67]. In this regard, in this paper, we establish an independent theoretical estimation, stimulating more accurate and well-designed experiment studies, such as employing large single crystals. We have calculated the optical phonon energy values (in meV) and the mode symmetries at Γ points at 300 K and classified them into three categories: Raman active (R) modes, infrared (IR) active modes, and nonactive modes (see Table S2 in Ref. [41]). On the other hand, the limitations of the theoretical approximation model are in aspects of (i) the thermal expansion effect, (ii) the anharmonic contributions to heat-flux [49], and (iii) higher-order phonon linewidths, such as four-phonon linewidths. Generally, feature (i) leads to an increasing lattice constant, as the positive Grüneisen parameters show (see Fig. S5 in the SM [41]). The thermal expansion effect softens the phonon frequencies and gives rise to decreased phonon lifetimes at high temperatures. However, the reduction of thermal expansion on κ_L can be partially counterbalanced by the increasing anharmonic contribution in heat flux at high temperatures [49,68]. Feature (ii), which naturally includes all anharmonic contributions, can be further studied by molecular dynamics simulation combined with machine learning but is not in the scope of this paper. However, we can assume that the result of molecular dynamics simulation could be slightly larger than our calculated values while maintaining the temperature dependence of the glassy κ_L due to the potential breakdown of the many-body perturbation theory, i.e., it generally overestimates the phonon broadening [69,70] and results in a reduced phonon lifetime in the PBTE framework. Our theoretical model does not include

feature (iii) since it has a weak impact on phonon transport in materials without optical-acoustical gaps [71] and the limitation of expensive computational costs. It is also expected that the additional four-phonon linewidths would lead to a slight reduction of κ_p and a modest enhancement of κ_c , thus an almost constant κ_L .

IV. CONCLUSIONS

In summary, we have investigated the microscopic mechanism of the glasslike lattice thermal conductivity in tetragonal α -CsCu₅Se₃, which exhibits ultralow $\kappa_L \sim 0.35\text{--}0.37$ W/mK. The SCPH method that considers the anharmonic phonon renormalization at finite temperatures induced by the quartic anharmonicity was utilized to analyze the phonon frequencies shift. The unified thermal transport theory of glass and crystal, which includes the contributions from particlelike and wavelike thermal channels (i.e., the diagonal and off-diagonal terms of heat flux), was employed to explore the low κ_L and its weak temperature-dependent behavior. Our results show that strong quartic anharmonicity induces phonon frequency hardening, giving rise to the decrease of phonon linewidths in acoustic and low-lying optical modes which is mainly associated with rattlinglike Cu3 atom vibration via reducing the available 3ph scattering phase space, thereby balancing the enhanced scattering rate as increasing phonon population when temperature induced and yielding a weak temperature-dependent κ_L . Strong phonon broadening leads to a strong coupling between interbranch coherent vibration eigenstates, resulting in a transformation from particlelike wave packet propagation to wavelike phonon transport in the dominance of heat transport. These findings highlight the role of the high-order anharmonicity in strong anharmonic complex systems, simulate the development of the disordered lattice dynamics, and provide the microscopic interpretation of the glasslike lattice thermal conductivity. Our results also supply theoretical guidance for the rational design of thermoelectric materials with ultralow lattice thermal conductivity for various energy applications.

ACKNOWLEDGMENTS

The authors gratefully acknowledge financial support from the National Natural Science Foundation of China (Grants No. 12074381, No. 12104458, and No. 12204482) and Guangdong Basic and Applied Basic Research Foundation (Grants No. 2021A1515110587 and No. 2022A1515140030). The authors also thank the computational resources from the Supercomputer Centre of the China Spallation Neutron Source.

[1] L. E. Bell, *Science* **321**, 1457 (2008).
 [2] G. J. Snyder and E. S. Toberer, *Nat. Mater* **7**, 105 (2008).
 [3] J. R. Sootsman, D. Y. Chung, and M. G. Kanatzidis, *Angew. Chem. Int. Ed.* **48**, 8616 (2009).
 [4] M. Beekman, D. T. Morelli, and G. S. Nolas, *Nat. Mater* **14**, 1182 (2015).
 [5] D. G. Cahill, S. K. Watson, and R. O. Pohl, *Phys. Rev. B* **46**, 6131 (1992).
 [6] P. B. Allen and J. L. Feldman, *Phys. Rev. Lett.* **62**, 645 (1989).

[7] P. B. Allen and J. L. Feldman, *Phys. Rev. B* **48**, 12581 (1993).
 [8] T. Tadano, Y. Gohda, and S. Tsuneyuki, *Phys. Rev. Lett.* **114**, 095501 (2015).
 [9] T. Tadano and S. Tsuneyuki, *Phys. Rev. Lett.* **120**, 105901 (2018).
 [10] D. J. Voneshen, K. Refson, E. Borissenko, M. Krisch, A. Bosak, A. Piovano, E. Cemal, M. Enderle, M. J. Gutmann, M. Hoesch *et al.*, *Nat. Mater* **12**, 1028 (2013).

- [11] Y. Xia, V. Ozoliņš, and C. Wolverton, *Phys. Rev. Lett.* **125**, 085901 (2020).
- [12] L. Isaeva, G. Barbalinardo, D. Donadio, and S. Baroni, *Nat. Commun.* **10**, 3853 (2019).
- [13] S. Mukhopadhyay, D. S. Parker, B. C. Sales, A. A. Puretzky, M. A. McGuire, and L. Lindsay, *Science* **360**, 1455 (2018).
- [14] M. Beekman and D. G. Cahill, *Cryst. Res. Technol.* **52**, 1700114 (2017).
- [15] J. L. Cohn, G. S. Nolas, V. Fessatidis, T. H. Metcalf, and G. A. Slack, *Phys. Rev. Lett.* **82**, 779 (1999).
- [16] G. S. Nolas, J. L. Cohn, G. A. Slack, and S. B. Schujman, *Appl. Phys. Lett.* **73**, 178 (1998).
- [17] J. S. Tse, V. P. Shpakov, V. R. Belosludov, F. Trouw, Y. P. Handa, and W. Press, *Europhys. Lett.* **54**, 354 (2001).
- [18] W. Li and N. Mingo, *Phys. Rev. B* **89**, 184304 (2014).
- [19] M. Christensen, A. B. Abrahamsen, N. B. Christensen, F. Juranyi, N. H. Andersen, K. Lefmann, J. Andreasson, C. R. H. Bahl, and B. B. Iversen, *Nat. Mater* **7**, 811 (2008).
- [20] F. Bridges and L. Downward, *Phys. Rev. B* **70**, 140201(R) (2004).
- [21] Q. Xi, Z. Zhang, J. Chen, J. Zhou, T. Nakayama, and B. Li, *Phys. Rev. B* **96**, 064306 (2017).
- [22] S. Christensen, M. S. Schmøkel, K. A. Borup, G. K. H. Madsen, G. J. McIntyre, S. C. Capelli, M. Christensen, and B. B. Iversen, *J. Appl. Phys.* **119**, 185102 (2016).
- [23] J. Tillman, *Nature (London)* **178**, 508 (1956).
- [24] Y. Luo, X. Yang, T. Feng, J. Wang, and X. Ruan, *Nat. Commun* **11**, 2554 (2020).
- [25] D. G. Cahill and R. O. Pohl, *Solid State Commun.* **70**, 927 (1989).
- [26] F. Zhou, W. Nielson, Y. Xia, and V. Ozoliņš, *Phys. Rev. Lett.* **113**, 185501 (2014).
- [27] F. Zhou, W. Nielson, Y. Xia, and V. Ozoliņš, *Phys. Rev. B* **100**, 184308 (2019).
- [28] F. Zhou, B. Sadigh, D. Åberg, Y. Xia, and V. Ozoliņš, *Phys. Rev. B* **100**, 184309 (2019).
- [29] T. Tadano and S. Tsuneyuki, *Phys. Rev. B* **92**, 054301 (2015).
- [30] I. Errea, B. Rousseau, and A. Bergara, *Phys. Rev. Lett.* **106**, 165501 (2011).
- [31] M. Simoncelli, N. Marzari, and F. Mauri, *Nat. Phys* **15**, 809 (2019).
- [32] Z. Zhang, Y. Guo, M. Bescond, J. Chen, M. Nomura, and S. Volz, *npj Comput. Mater.* **8**, 96 (2022).
- [33] N. Ma, Y.-Y. Li, L. Chen, and L.-M. Wu, *J. Am. Chem. Soc.* **142**, 5293 (2020).
- [34] P. Hohenberg and W. Kohn, *Phys. Rev.* **136**, B864 (1964).
- [35] P. E. Blöchl, *Phys. Rev. B* **50**, 17953 (1994).
- [36] G. Kresse and J. Furthmüller, *Phys. Rev. B* **54**, 11169 (1996).
- [37] J. P. Perdew, A. Ruzsinszky, G. I. Csonka, O. A. Vydrov, G. E. Scuseria, L. A. Constantin, X. Zhou, and K. Burke, *Phys. Rev. Lett.* **100**, 136406 (2008).
- [38] K. Esfarjani and H. T. Stokes, *Phys. Rev. B* **77**, 144112 (2008).
- [39] A. Togo, and I. Tanaka, *Scripta Mater.* **108**, 1 (2015).
- [40] E. J. Candes and M. B. Wakin, *IEEE Signal Process. Mag.* **25**, 21 (2008).
- [41] See Supplemental Material at <http://link.aps.org/supplemental/10.1103/PhysRevB.108.014302> for convergence tests of the calculated κ_p concerning q -point mesh, convergence tests of the calculated κ_p at 300 K with low and high AIMD simulation, convergence tests of the calculated κ_p with different numbers of configurations, the calculated temperature-dependent anisotropic MSDs and equivalent isotropic displacement parameter U_{eq} of different atoms, The Cu3 atom-resolved phonon density of states for harmonic approximation and different temperatures, three-dimensional visualizations of the mode-specific contributions to the coherent thermal conductivity at 50 K, the calculated Gruneisen parameters and the calculated optical phonon energy values (in meV), and the mode symmetries at Γ at 300 K.
- [42] L. J. Nelson, G. L. W. Hart, F. Zhou, and V. Ozoliņš, *Phys. Rev. B* **87**, 035125 (2013).
- [43] Y. Xia, *Appl. Phys. Lett.* **113**, 073901 (2018).
- [44] K. Pal, Y. Xia, and C. Wolverton, *npj Comput. Mater.* **7**, 5 (2021).
- [45] T. Tadano, Y. Gohda, and S. Tsuneyuki, *J. Phys.: Condens. Matter* **26**, 225402 (2014).
- [46] Q.-Y. Xie, J.-J. Ma, Q.-Y. Liu, P.-F. Liu, P. Zhang, K.-W. Zhang, and B.-T. Wang, *Phys. Chem. Chem. Phys.* **24**, 7303 (2022).
- [47] Q.-Y. Xie, P.-F. Liu, J.-J. Ma, F.-G. Kuang, K.-W. Zhang, and B.-T. Wang, *Materials* **15**, 3147 (2022).
- [48] W. Lv and A. Henry, *Sci. Rep* **6**, 35720 (2016).
- [49] R. J. Hardy, *Phys. Rev.* **132**, 168 (1963).
- [50] H. Lin, G. Tan, J.-N. Shen, S. Hao, L.-M. Wu, N. Calta, C. Malliakas, S. Wang, C. Uher, C. Wolverton *et al.*, *Angew. Chem. Int. Ed.* **55**, 11431 (2016).
- [51] W. Li, J. Carrete, N. A. Katcho, and N. Mingo, *Comput. Phys. Commun.* **185**, 1747 (2014).
- [52] P.-F. Liu, T. Bo, J. Xu, W. Yin, J. Zhang, F. Wang, O. Eriksson, and B.-T. Wang, *Phys. Rev. B* **98**, 235426 (2018).
- [53] R. Peierls, *Ann. Phys.* **395**, 1055 (1929).
- [54] X.-L. Zhu, P.-F. Liu, J. Zhang, P. Zhang, W.-X. Zhou, G. Xie, and B.-T. Wang, *Nanoscale* **11**, 19923 (2019).
- [55] X. Li, P.-F. Liu, E. Zhao, Z. Zhang, T. Guidi, M. D. Le, M. Avdeev, K. Ikeda, T. Otomo, M. Kofu *et al.*, *Nat. Commun.* **11**, 942 (2020).
- [56] Z. Liu, J. Mao, J. Sui, and Z. Ren, *Energy Environ. Sci.* **11**, 23 (2018).
- [57] X.-L. Zhu, C.-H. Hou, P. Zhang, P.-F. Liu, G. Xie, and B.-T. Wang, *J. Phys. Chem. C* **124**, 1812 (2020).
- [58] L.-D. Zhao, S.-H. Lo, Y. Zhang, H. Sun, G. Tan, C. Uher, C. Wolverton, V. P. Dravid, and M. G. Kanatzidis, *Nature (London)* **508**, 373 (2014).
- [59] S. Karak, J. Bera, S. Paul, S. Sahu, and S. Saha, *Phys. Rev. B* **104**, 195304 (2021).
- [60] P. G. Klemens, *Phys. Rev.* **148**, 845 (1966).
- [61] Y. Xia, K. Pal, J. He, V. Ozoliņš, and C. Wolverton, *Phys. Rev. Lett.* **124**, 065901 (2020).
- [62] H. Shao, D. Ding, Y. Fang, W. Song, J. Huang, C. Dong, and H. Zhang, *Phys. Rev. B* **107**, 085202 (2023).
- [63] P. B. Allen, J. L. Feldman, J. Fabian, and F. Wooten, *Philos. Mag. B* **79**, 1715 (1999).
- [64] L. L. Huang, Y. S. Wang, C. Zhu, R. Xu, J. M. Li, J. H. Zhang, D. Li, Z. M. Wang, L. Wang, C. J. Song *et al.*, *J. Alloys Compd.* **769**, 478 (2018).
- [65] K. Suekuni, C. H. Lee, H. I. Tanaka, E. Nishibori, A. Nakamura, H. Kasai, H. Mori, H. Usui, M. Ochi, T. Hasegawa *et al.*, *Adv. Mater.* **30**, 1706230 (2018).

- [66] H. Liu, X. Shi, F. Xu, L. Zhang, W. Zhang, L. Chen, Q. Li, C. Uher, T. Day, and G. J. Snyder, *Nat. Mater.* **11**, 422 (2012).
- [67] P. Vaquero, G. Guélou, A. Kaltzoglou, R. I. Smith, T. Barbier, E. Guilmeau, and A. V. Powell, *Chem. Mater.* **29**, 4080 (2017).
- [68] T. Sun and P. B. Allen, *Phys. Rev. B* **82**, 224305 (2010).
- [69] A. Glensk, B. Grabowski, T. Hickel, J. Neugebauer, J. Neuhaus, K. Hradil, W. Petry, and M. Leitner, *Phys. Rev. Lett.* **123**, 235501 (2019).
- [70] U. Aseginolaza, R. Bianco, L. Monacelli, L. Paulatto, M. Calandra, F. Mauri, A. Bergara, and I. Errea, *Phys. Rev. Lett.* **122**, 075901 (2019).
- [71] N. K. Ravichandran and D. Broido, *Phys. Rev. X* **10**, 021063 (2020).